

1 **Optimization of Processing Parameters for Waterjet-Guided Laser**

2 **Machining of SiC/SiC Composites**

3 Mengxuan Gao^a, Songmei Yuan^{a,b,*}, Jiayong Wei^a, Jin Niu^c, Zikang Zhang^a, Xiaoqi Li^a, Jiaqi Zhang^a,
4 Ning Zhou^a, Mingrui Luo^d

5

6 ^a R&D Center of High-efficient & Green CNC Machining Technology and Equipment, School of
7 Mechanical Engineering and Automation, Beihang University, Beijing, 100191, China

8 ^b Ningbo Institute of Technology, Beihang University, Ningbo, 315832, China

9 ^c Department of Computer Science, University of British Columbia (UBC), Vancouver, Canada

10 ^d The School of Artificial Intelligence, University of Chinese Academy of Sciences, Beijing 100049,
11 China

12 * Corresponding author: Beihang University, No. 37 Xueyuan Road, Beijing, 100191, China.

13 Email address: yuansm@buaa.edu.cn (S. Yuan).

14

15 **Abstract**

16 Interactions between light and matter during short-pulse water-jet guided laser materials
17 processing are highly nonlinear, and acutely sensitive to laser machining parameters. Traditionally,
18 the physical simulation calculation methods based on laser, water and composite materials are
19 complicated. This work combines neural networks and physical simulation models in the
20 understanding of laser drilling of composite materials. Neural networks are used to predict SiC/SiC
21 composites laser drilling results by using processing parameters (average power, scanning speed,
22 and filling spacing) as input parameters, optimal combinations of processing parameters based on
23 the neural network are identified, and the effectiveness of the learned knowledge is validated using
24 a physical simulation model. The results show that the neural network can identify the nonlinear
25 effect of processing parameters on machining quality with the MAE of 0.054 and the RMSE of
26 0.067. The physical simulation model could explain why this nonlinear effect exists. This method
27 can be applied to a wide range of fields. In the face of unknown material and physical processing
28 processes, the approach of combining neural networks and physical simulation models has the
29 potential to significantly reduce the optimization time and deepen the understanding of laser
30 processing.

31 **Keywords**

32 SiC_f/SiC composites, Laser machining, Physical simulation, Neural networks, Micro-
33 structuring, Parameter optimization

34

1 1. Introduction

2 With the rapid development of aerospace technology, the requirements for the performance of
3 materials in the hot-end components have gradually increased. There is an urgent need for new
4 materials with good mechanical, physical, and heat-resistant properties (An et al., 2021; Gavalda
5 Diaz et al., 2019). SiCf/SiC material, as a new type of high-strength and high-temperature resistant
6 ceramic, has the characteristics of low density ($2\text{--}3 \text{ g/cm}^3$), high-temperature resistance
7 ($>1500^\circ\text{C}$), corrosion resistance, and excellent mechanical properties. However, the processing of
8 ceramic-based materials is extremely difficult (Bilal et al., 2018; Samant & Dahotre, 2009).
9 Researchers consider using laser to process SiCf/SiC materials.

10 Special machining technologies for this material include abrasive water-jet machining (AWJ),
11 electrical discharge machining (EDM), ultrasonic machining, and laser beam machining (LBM)
12 (An et al., 2021; Gavalda Diaz et al., 2019). Laser processing has advantages over the above
13 methods, embodied in its good processing quality, non-contact processing, low input heat to
14 materials, and ease of combination with numerical control technology. Among various approaches
15 of laser processing, water-jet guided nanosecond lasers (Porter et al., 2007; Sun et al., 2019) have
16 balanced processing accuracy and efficiency.

17 There are many adjustable water-jet guided laser processing parameters (Bakhtiyari et al., 2021)
18 (such as laser power, repetition rate, scanning speed and machining path spacing). These laser
19 processing parameters will act on the processing results in a nonlinear relationship (Ciurana et al.,
20 2009; Goeke & Emmelmann, 2010). Identifying these parameters without enough experiments and
21 accurate physical models is difficult.

22 One method to investigate the influence of processing parameters on processing results is to
23 establish a physical model for the entire laser processing process based on physical simulations of
24 laser, water, and composite materials, after fully understanding the interaction between materials in
25 laser processing. In many fields, including but not limited to manufacturing (Jiang et al., 2016; Ren
26 et al., 2023), the engineering tasks can be adequately expressed using physical models, and in such
27 cases, the significance of neural networks is limited. Unfortunately, current simulations are only
28 available for laser drilling simulations of metal materials (Shen et al., 2001; Y. Zhang et al., 2013,
29 2014). We may also need to consider issues such as the removal and deformation of anisotropic
30 composites, plasma generation, and multiphoton interaction to obtain simulation accuracy, which is
31 usually impossible. In addition, some important physical processes in water-jet guided laser
32 processing may even be unknown to us. These reasons make it difficult for physical models to
33 establish., but it's possible to simulate some experimental results and trends.

34 Another approach is to try as many combinations of processing parameters as possible within the
35 optional parameter range. If we take 10 levels for each parameter, for the combinations of three
36 parameters, there will be 1000 experiments need to be done. Considering the stability of the
37 processing equipment, it is impossible to try all parameter combinations and observe and analyze
38 the results.

39 Considering the complexity of collecting experimental data in materials science, using small
40 samples and neural networks as an alternative has become popular (L. Chen et al., 2023; Feng et al.,
41 2019; Y. Zhang & Ling, 2018). In laser processing, this approach has been proven to be very
42 effective in predicting the surface morphology of the processed material (Casalino, 2018; Heath,

1 Grant-Jacob, Eason, et al., 2018; Heath, Grant-Jacob, Xie, et al., 2018; Liao et al., 2023; McDonnell
2 et al., 2021; Y. Zhang, 2023). Some research also indicates that neural networks can learn physical
3 rules from datasets and simulate physical phenomena without an explicit physical description
4 equation for a system (Mills et al., 2018; F. Wang et al., 2020; S. Xie et al., 2023; Z. Xie et al., 2023).
5 Therefore, using artificial neural networks to help us optimize the parameters and verify with the
6 physical model is necessary.

7 Artificial neural networks (ANNs) are a type of neural network inspired by biology, typically
8 consisting of input, hidden, and output layers, each containing a certain number of neurons
9 connected layer by layer. Generally, the input and output of an artificial neural network are one-
10 dimensional vectors, and each neuron in the network contains a connection weight of w and a bias
11 of b for each layer. After the neural network processes the input vector, the neural network updates
12 the connection weights and biases by calculating the difference between the output vector and the
13 actual training data. This updating process is called backpropagation (BP). The theory behind neural
14 networks can be found in the book *Deep Learning* (Goodfellow I, Bengio Y, & Courville A., 2016).
15 This article uses process parameters data as the neural network input and quality parameters extracts
16 from the results of optical microscope images as output labels. Artificial neural networks (ANN)
17 and machine learning method have been continuously colliding with traditional research fields in
18 recent years, sparking new advancements and applications. These include machining (Hamrani et
19 al., 2023; Huang et al., 2023; Rong et al., 2016), material performance prediction (J. Yang et al.,
20 2023), infectious disease prediction (Manohar & Das, 2022, 2023), depression diagnosisand(M. Li
21 et al., 2023), and more.

22 In previous works, Yousef (Yousef et al., 2003) used ANN to predict the laser pulse energy
23 required to achieve a specific depth and diameter of a pit. Casalino (Casalino et al., 2017) used pulse
24 frequency, pulse width, and laser power as input parameters to optimize the machining parameters.
25 The input and output were the average diameter and taper of the input and output. In another paper,
26 Casalino (Casalino et al., 2016) optimized the process by using welding speed and shielding gas
27 type as input and fusion zone, weld width, melt depth, and porosity area as output. Rong (Rong et
28 al., 2016) addresses the multi-objective optimization of bead profile, and the average prediction
29 error is 9.95 and 8.54 %. Chaki (Chaki et al., 2020) uses the ANN-NSGA model to predict the
30 roughness and material removal rate of laser cutting. The model takes cutting speed, pulse energy,
31 and pulse width as inputs. McDonnell (McDonnell et al., 2021) apply neural networks for parameter
32 optimization and for predictive visualisation of expected outcomes in laser surface texturing with
33 blind vias for tribology control applications.

34 Although the articles above are not explicitly focused on hole drilling, they all address
35 optimization problems in mechanical processing. Most of these articles utilize ANN neural
36 networks as models and have achieved good predictive results. However, they have some issues:
37 1. Limited sample size: The datasets used in these studies typically consist of only around 30 data
38 points. 2. Lack of physical explanation in parameter selection: One crucial aspect is the absence of
39 associated physical models, resulting in a lack of physical interpretation for parameter selection.
40 Neural networks are black-box models (Kashinath et al., 2021). Therefore, alongside providing
41 parameter choices, it is essential to incorporate physical models for validation and to offer
42 reasonable explanations for parameter selections.

43 In response to the issues above, this paper specifically designs a machining task and establishes
44 a neural network model and a physical simulation model. The input parameters for the neural

1 network are combinations of processing parameters, and the output parameters are quality
2 parameters. The quality parameter labels in the dataset are extracted from optical microscope
3 images of the machining results. A physical model is established based on the machining process
4 of this task. Like the neural network, this physical simulation model takes two processing
5 parameters (laser power: 4-20 W and scan path spacing: 30-70 mm/s) as inputs. The model
6 produces a finite element calculation result as the output. By synchronously adjusting the inputs of
7 the neural network and the physical model, we can observe the impact of changes in processing
8 parameters on the processing results in both the neural network and the physical model. This
9 provides a physical interpretation for parameter selection based on the neural network. This
10 approach facilitates a deeper understanding of the machining process. Instead of relying solely on
11 neural networks for prediction, a more valuable research approach would involve the integration
12 of neural networks, physical models, and experiments.

13 The paper is organized as follows: Chapter 2 is divided into three parts, and introduces the
14 material and water-guided laser ablation experimental design, the process of experimental data
15 processing, and the establishment of the physical simulation model. Chapter 3 is also divided into
16 three parts. Firstly, we discuss the accuracy of predictions using various traditional machine
17 learning algorithms and our neural network. Secondly, based on the optimal ANN model, we
18 apply the GA (genetic algorithm) to find the best combination of processing parameters. Finally,
19 we analyze the influence of different processing parameters on the quality parameters according to
20 the established physical model. Chapter 4 concludes the paper.

21

22

23

24

2. Experimental and calculation details

In order to obtain an improved set of processing parameters, a visualization-based objective optimization method was established using backpropagation neural networks. Additionally, the parameter selection was validated and explained using a finite element physical model. The flowchart of the entire analysis process is shown in Figure 1, which includes the experimental phase, prediction and optimization phase, and verification and explanation phase.

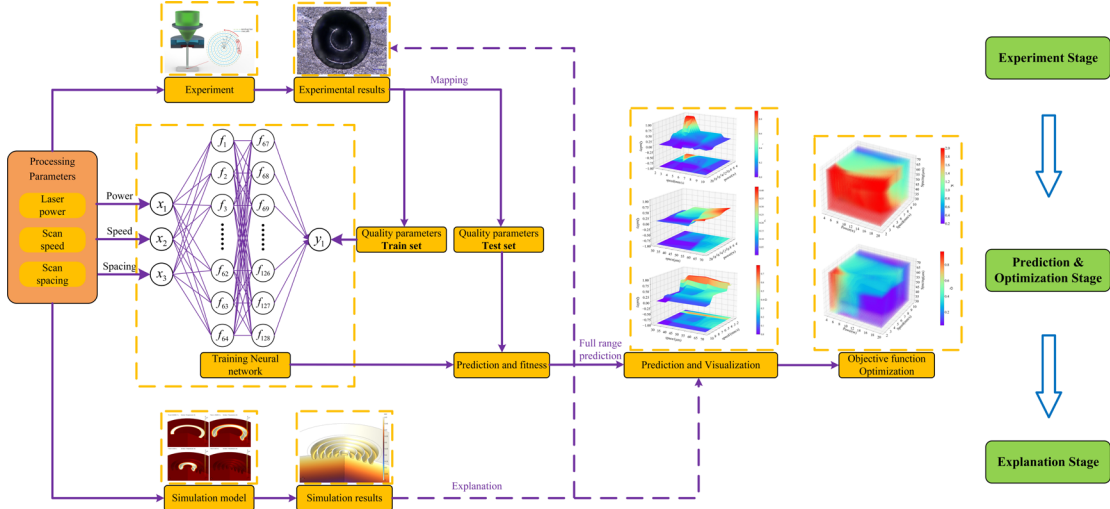


Fig. 1. Flow chart of optimization of the waterjet-laser machining

2.1 Material

The MI process prepared the SiCf/SiC composites used in this paper at Central South University (Changsha). The material uses SiC fibers alternately laid horizontally and vertically as a reinforcement material, and the fiber volume fraction is about 40%. The schematic diagram of its structure is shown in Figure 1(a). The properties and parameters of SiCf/SiC composites are shown in Table 1. All materials are sanded with micron sandpaper and ultrasonically cleaned with alcohol before machining. The cleaned surface is shown in Fig. 1(b).

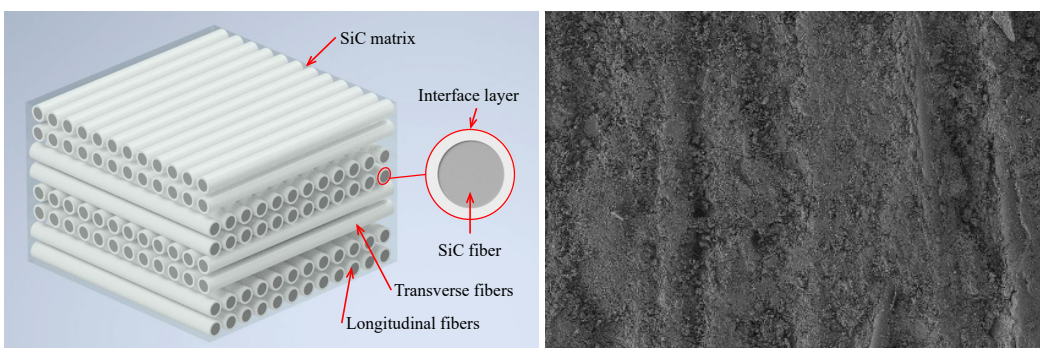


Fig. 2. 2D SiC/SiC composites: (a) diagram of its structure; (b) surface after polishing and ultrasonic cleaning

1

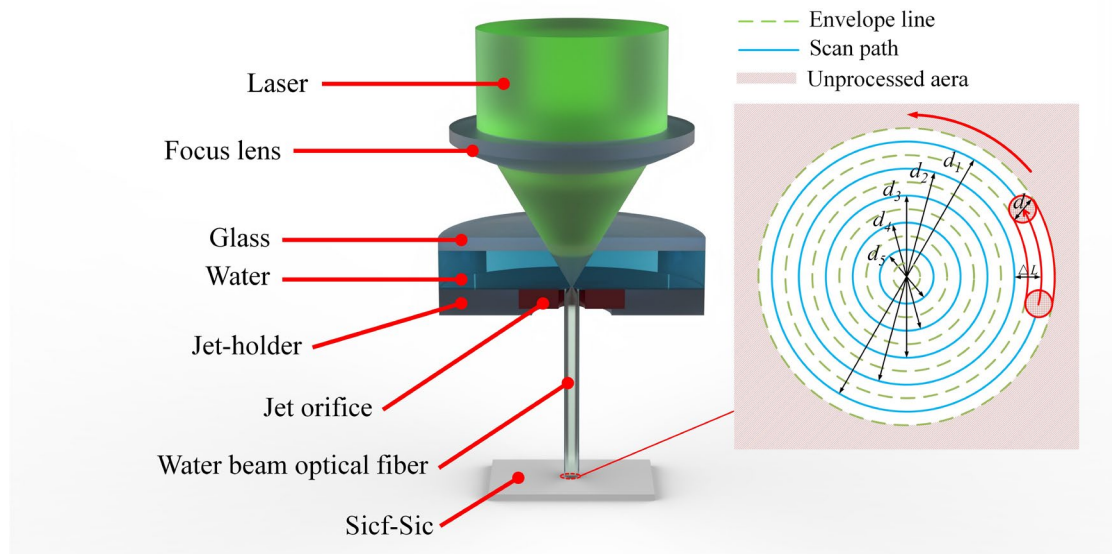
Table 1 Properties and parameters of the SiCf/SiC composites

Parameters	Value
Density	2.5 g/mm ³
Thickness of interface layer	~300 nm
Diameter of SiC fiber	~12μm
Interlayer spacing	200μm
Fiber volume fraction	~40%
Porosity	~2%
Sample size	20*20*3 mm ³

2

3 **2.2 Waterjet-guided laser ablation experiment**

4 In the aerospace field, it is necessary to create small holes with a diameter of 0.5mm on the hot
 5 end components to increase the heat dissipation area and reduce the weight of the components. Due
 6 to the small focal diameter of the water jet laser, this kind of hole processing usually requires the
 7 laser drilling system to remove material in a circular scanning pattern, layer by layer, to ultimately
 8 form holes of approximately 0.5mm in diameter. This experiment used the LCS305 waterjet-guided
 9 laser processing machine tool from Synova to drilling the SiCf/SiC composite materials. The system
 10 is capable of micro-nano machining with complex features such as drilling and cutting, as shown in
 11 Fig. 2. The wavelength of the Nanosecond waterjet-guided laser (Diode pumped solid state Nd:
 12 YAG, pulsed) is 532 nm, the pulse width is 240 ns, and the repetition frequency is 6 kHz. Its
 13 scanning system can focus the beam on the upper surface of the SiCf/SiC composite material in a
 14 spot with $d = 50 \mu\text{m}$ diameter. The machining process is set as circular scanning, and the first and
 15 largest circular scanning diameter is $d_1 = 500 \mu\text{m}$. The next scanning ring's diameter is reduced
 16 according to the spacing (ΔL). If the spacing is 50 μm, then the scanning diameters are 400, 300,
 17 200, and 100 μm. Other processing parameters that can be changed include a scanning speed(V) of
 18 2–10 mm/s, and an average laser power (P) of 4–20 W, refer to Table 2. The typical values are
 19 spacing for 50 μm, scanning speed of 6 mm/s, and average power of 8 W. Since the laser spot has a
 20 diameter of $d = 50 \mu\text{m}$, the ideal diameter of the final machined hole is about 550 μm (laser spot
 21 diameter d plus largest circular scanning diameter d_1). After processing, use an optical microscope
 22 and a KEYENCE VHX-5000 ultra-depth microscope to observe the shape of the micropores and
 23 take pictures.



1

2 Fig. 3. Specialized system for Waterjet-Guided laser ablation of SiCf/SiC composites

3 Table 2 Full range of parameters for investigation

4

5 **2.3. Data processing**

6 After collecting the optical microscope pictures of the processing results, the next step is to use
 7 data processing methods to extract the processing quality parameters. It can be observed that there
 8 is a multi-layered ring structure inside the small hole, as shown in Fig.4, a possible reason for the
 9 formation of this structure is the combination of low laser power, high scanning speed and large
 10 scanning spacing. The reflective area along the edge of the hole is due to the steep slope of the hole
 11 wall. In order to explore the specific reasons for its appearance and understand the coupling
 12 relationship between various processing parameters, it's necessary to quantify it as a processing
 13 quality parameter, and establish a neural network to correlate it with laser processing parameters
 14 (power, scanning speed, spacing).

15 The quantifying process is as follows: convert the optical microscope images into a grayscale
 16 image, and then use the Hough Circles detection module in the OpenCv library to frame the
 17 processing hole in the images, and reset the part outside the Hough Circles to black pixels. Now
 18 only the internal structure of the small hole remains in the picture. There are two cases of white
 19 pixels inside the small hole: rings and reflections caused by the slope of the hole wall, both of which
 20 are undesirable in laser processing. Sum these white parts in units of pixels, and divide all the
 21 number of pixels in the hole to get the quality parameter of the small hole. After normalization, the
 22 quality parameter can be compressed to numbers between 0–1, where 0 represents the best processed
 23 small hole (no surface structure and sloping pore wall), and 1 represents the worst processed small
 24 hole. According to data set, the quality parameter in the 0–0.4 range is small holes with small wall
 25 taper and a small number of rings or no rings. The small holes with quality parameters above 0.5–
 26 0.8 have multiple ring structures.

1 In the traditional laser machining of through-hole, if you want to examine the slope of the hole
 2 wall and the diameter of the entrance and exit, you can cut the hole wall along the diameter direction,
 3 or process on the edge of the material to observe the internal shape of the small hole. However, if
 4 the small hole is cut in half, this ring structure will be destroyed, and this why this work chose a
 5 composite parameter (quality parameters) that reflects both the structure of the multiple rings and
 6 the slope of the wall.

7 In addition, the ring structure is generally incomplete under the scour of high-pressure water jets.
 8 The process of water jet scouring and destroying the ring structure is highly random and difficult to
 9 simulate. Therefore, for the same combinations of processing parameters, the experiments repeat
 10 multiple times to reduce the randomness.

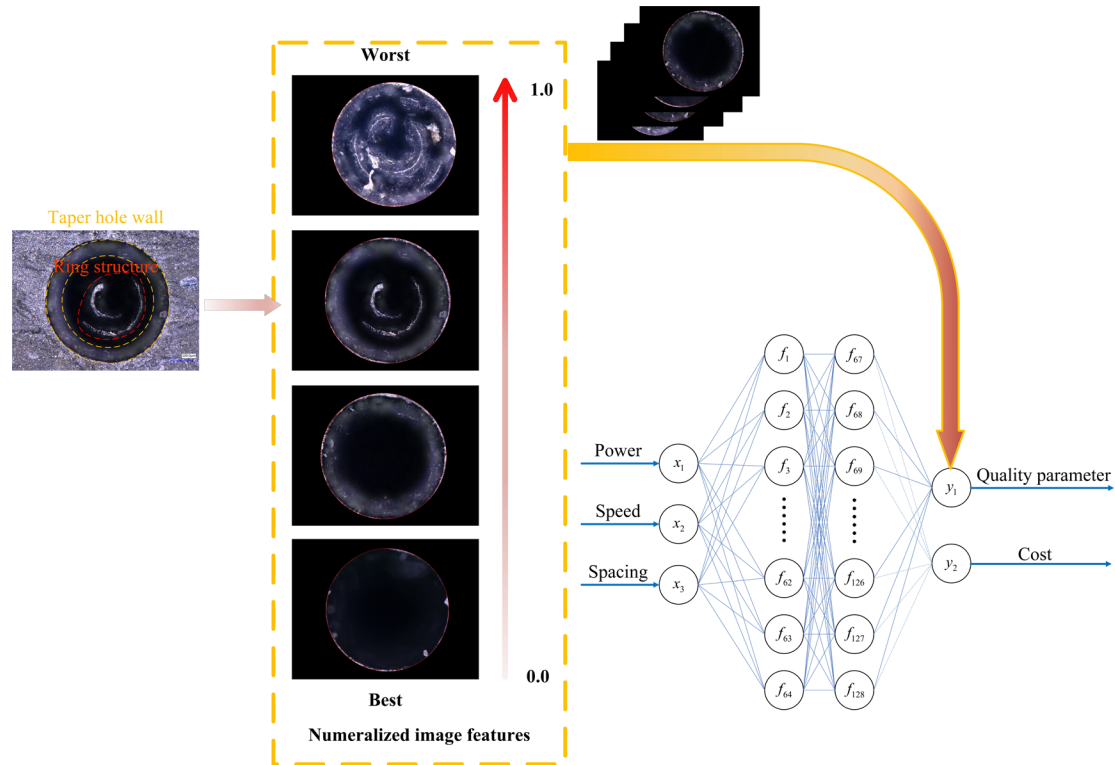


Fig. 4. Generating quality parameters from experimental results

12 The original data set of the experiment is 300 and 30% of the dataset is set to be the test dataset
 13 (90). In order for the neural network to mine more information and simulate actual processing data
 14 fluctuations, this work use a variety of data enhancement methods (setting different image
 15 binarization thresholds and adding Gaussian noise) to expand the training dataset (210) to 26680.
 16 The training set for the comparative algorithm was the same expanded dataset, while all the
 17 predicting models used the testset consisted of the original 90 test samples.

2.4. Physical simulation model

The parameter selection purely relying on the neural network lacks the support of the physical model, and it is not convincing in many cases. This section is to establish a physical model of waterjet-guided laser processing, although many physical processes were simplified in order to make sure that the physical model can be calculated by numerical calculation. For this physical model, three variable parameters (same as experiment parameters, Table 2) are provided, including power, scanning speed, and spacing.

Waterjet-guided laser belongs to nanosecond laser, the process of ablating materials conforms to Fourier's law of heat conduction. The equation heat conduction is shown as follows:

$$\rho C_p \frac{\partial T}{\partial t} = \nabla \cdot (k \nabla T) + A(z, t) + H_s \quad (1)$$

Where ρ is density, C_p is heat capacity, T is temperature, t is time, k is heat conductivity, A is laser heat source term, and H_s appears as a heat source term when energy associated with the latent heat of sublimation is being absorbed.

$$A(z,t) = I(t)[1 - R(T)]\alpha(T)e^{-\alpha(T)z} \langle \vec{n}, \vec{e}_z \rangle \quad (2)$$

$$I(t) = P(t) / \left(\pi d^2 / 4 \right) \quad (3)$$

Laser heat source A is related to the hole depth z and time t , and I is the laser power intensity, determined by laser power P and diameter d of the waterjet-guided laser beam, $R(T)$ is the reflectance of the material to the laser with temperature, $\alpha(T)$ is the absorption rate of the material to the laser with temperature, and $\langle \vec{n}, \vec{e}_z \rangle$ is the dot product of the unit normal vector of the ablative surface and the unit vector parallel to the z -axis. The rectangular wave shape of the laser power output $P(t)$ is sketched in Fig. 4, where τ is pulse length, and f is pulse frequency. Considering that in the waterjet-guided laser, the laser has many times total reflection and uniform distribution in the water beam, there is almost no energy lost by reflection, and the material completely absorbs the energy, so $\alpha(T)=1$, $R(T)=0$.

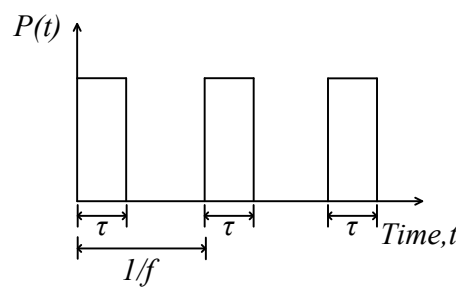


Fig. 5 Laser pulse output

Convection heat losses take place at the top surface of the workpiece, and the energy losses at boundaries are calculated by the use of

$$-kV T = -h \left[T - T_{amb} \right] \quad (4)$$

1 Where h is the convection coefficient, T_{amb} is the ambient temperature, the loss of radiation can
 2 be ignored. The other surfaces of the workpiece could be assumed insulated cause the size is well
 3 beyond the ablation surface. The high cooling effect of the water-jet can be calculated by empirical
 4 formula (C.-F. Li et al., 2003).

5 To demonstrate the ablation process, this work used a solid heat transfer (ht) and deformation
 6 geometry (dg) interface in Comsol, and used an event (ev) interface to control multiple ablations of
 7 the workpiece surface by pulsed laser.

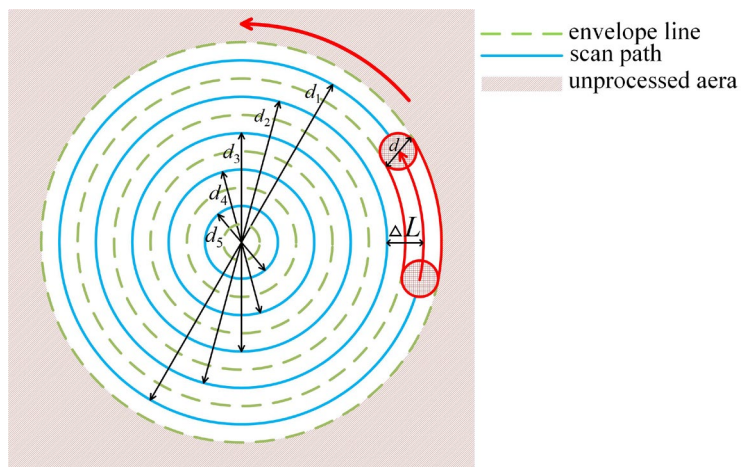
8 After the material has been heated to Ablation temperature, the laser energy is used to provide
 9 latent heat of sublimation (H_s), which can be stored in Comsol Multiphysics using Eq. (13) in the
 10 form of heat conduction. Eq. (14) is used to convert it into the deformation rate (v_a) of the top surface
 11 of the workpiece.

$$12 \quad q_a = h_a (T - T_a) \quad (5)$$

$$13 \quad v_a = \frac{q_a}{\rho \times H_s} \quad (6)$$

14 Considering the calculation time of the model at the nanosecond scale and the symmetry of
 15 processing model, this work established a r,z-two-dimensional axisymmetric model in Comsol
 16 Multiphysics, with a model size of 0.5 mm * 0.5 mm. The model uses free triangular mesh. In
 17 addition, considering that the diameter of the waterjet-guided laser spot is 50 μm , the mesh size at
 18 the upper surface of the model and the axis of symmetry is refined to 2 μm . Because this is a large
 19 deformation process, the finite element mesh will be remeshed when the mesh quality was less than
 20 0.2.

21 In order to integrate the laser scanning speed into the central symmetry model, refer Fig. 5.



22
 23 Fig. 6 Laser scanning path map

24 In this figure, for easy understanding, the spacing (ΔL) is set to 50 μm . The laser processing spot
 25 radius in the figure is $r = 25 \mu\text{m}$. The radius of the first processing path is $r_1 = 250 \mu\text{m}$, the radius of
 26 the second processing path is $r_2 = 200 \mu\text{m}$, the interval between the processing paths is the
 27 spacing(ΔL), and so on. The time it takes for the laser to go through the nth processing radius is:

$$28 \quad t_n = \frac{2\pi r_n}{v} \quad (7)$$

29 v is scanning speed, r_n is the radius of the nth scan path, t_n is the time it takes.

1 The ring area swept by the waterjet-guided laser is enclosed by the circle radius of r_n+r and the
 2 circle of r_n-r , so the heat flux of the laser on the nth track is as:

$$3 \quad I(t_n) = \frac{P(t_n)}{\pi(r_n + r)^2 - \pi(r_n - r)^2} = \frac{P(t_n)}{4\pi rr_n} \quad (8)$$

4 Finally this work integrated power, scan speed and spacing into the model, and the simulation is
 5 based on the following assumptions and Table 3 material properties:

- 6 (1) Plasma does not affect the transmission of waterjet-guided laser.
- 7 (2) Plasma formation and multiple reflection are not taken into consideration.
- 8 (3) SiC resublimation accumulation is not considered.
- 9 (4) High-pressure water-jet only considers its cooling effect(C.-F. Li et al., 2003), and the
 10 strong erosion and damage effect on the surface structure is not considered.
- 11 (5) The laser power intensity at the workpiece is uniform throughout the cross-section of the
 12 water-jet guided laser.
- 13 (6) The thermal conductivity k and specific heat C_p do not change with temperature.
- 14 (7) Because the orientation of the fiber does not affect the macroscopic structure, the
 15 composite material is equivalent to the homogeneous material.

16 Table 3 material properties

Property	Value(J. Chen et al., 2021; Z. Li et al., 2020; H. Wang et al., 2010; Wei et al., 2022)
Density [kg/m ³]	2500
Thermal conductivity [W/(m·K)]	10.6
Specific heat capacity [J/(kg·K)]	350
Latent heat of sublimation [kJ/kg]	9975
Ablation temperature [K]	2973.15
Ambient temperature [K]	293.15

17
 18
 19
 20
 21

1 **3. Results and discussion**

2 **3.1 Machine learning methodology**

3 The ANN network model used in this work has a structure shown in Fig. 6, consisting of three
4 dense layers, also known as fully connected layers. Each dense layer had a ReLU activation
5 function. The number of neurons in each fully connected layer is determined by a genetic algorithm
6 from the geatpy library in Python(L. Yang & Shami, 2020), with 64 neurons. The input parameters
7 of the neural network are a vector of parameters: laser power, scanning speed, and fill spacing.
8 Before inputting the parameters, considering the issue of parameter magnitude, these three
9 parameters will be normalized according to Table 4, mapping them to a range between 0 and 1. The
10 output parameter is a single-value vector of the machining quality parameters defined in Section 2.3.
11 Therefore, the number of neurons in each fully connected layer of the network is (3, 64), (64, 64),
12 and (64, 1), respectively. The optimizer chosen is AdamW(Loshchilov & Hutter, 2019), and the loss
13 function is MSEloss. This work used WandB for hyperparameter search and determined the values
14 for epoch number, learning rate, and batch size. The search range for batch size was set to 64, 128
15 and 256; The range for learning rate was set to 0.01, 0.005, 0.002, 0.001, 0.0005, 0.0002 and 0.0001;
16 The range for epoch was set to 0, 75, 100, 125, 150, 175 and 200; Finally, the neural net work
17 obtained the best combination of hyperparameters with batch size for 64, learning rate for 0.005 and
18 epoch number for 100.

19 Table 4 Normalized value of experimental input parameters

Factors	Normalized value				
	0	0.25	0.5	0.75	1
Average power /W	4	8	12	16	20
Scanning speed /(mm/s)	2	4	6	8	10
Spacing /(μm)	30	40	50	60	70

20 The entire training process of the neural network for 100 epochs takes about 37 seconds. When
21 training is completed, the saved network can output the machining quality parameters for a vector
22 of machining parameters input: power, speed, and scan spacing.

23

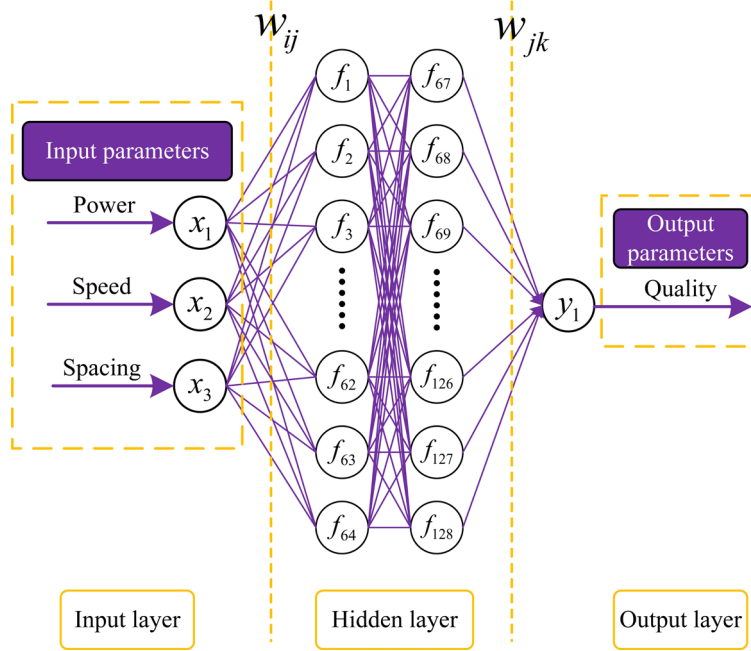


Fig. 7 Neural network structure

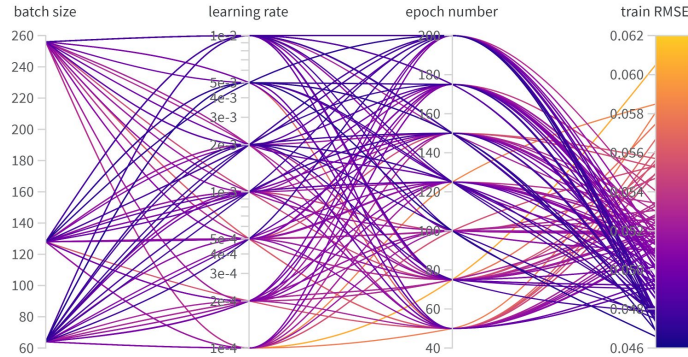


Fig. 8 Hyper-parameters search

5 The convergence process of the model is shown in Fig. 8. The RMSE_loss graph shows that the
 6 training set RMSE was about 0.14 at the beginning, then ,after 20 rounds of training, dropped to
 7 about 0.05. After that, with the lowest RMSE at around 0.046-0.05. The test set RMSE followed a
 8 similar pattern to the training set, with an initial RMSE of about 0.17, and the RMSE of the test set
 9 is about 0.08 in rounds 20, finally, The RMSE value is still fluctuating between 0.063 and 0.076.



Fig. 9 Convergence process of the model

To evaluate the performance of the ML models, two evaluation metrics, mean absolute error (MAE), and root mean squared error (RMSE), are introduced in this work. They are defined as:

$$MAE = \frac{1}{N} \sum_{i=1}^N |y_i - p_i| \quad (9)$$

$$RMSE = \sqrt{\frac{1}{N} \sum_{i=1}^N (y_i - p_i)^2} \quad (10)$$

where N is the number of the dataset, y_i and p_i represent the i th true and predicted value.

In order to compare the performance of the NN model, this work utilized the sklearn library to call three modern regression models: Support Vector Regression (SVR), Random Forest Regression (RFR), and XGBoost Regression (XGBR). The comparison results are shown in Table 4.

Table 5 ML model Comparison results

Model	RMSE	MAE
NN	0.0668	0.0536
Support Vector Regression	0.1034	0.0775
Random Forest Regression	0.0701	0.0553
XGBoost Regression	0.0690	0.0554

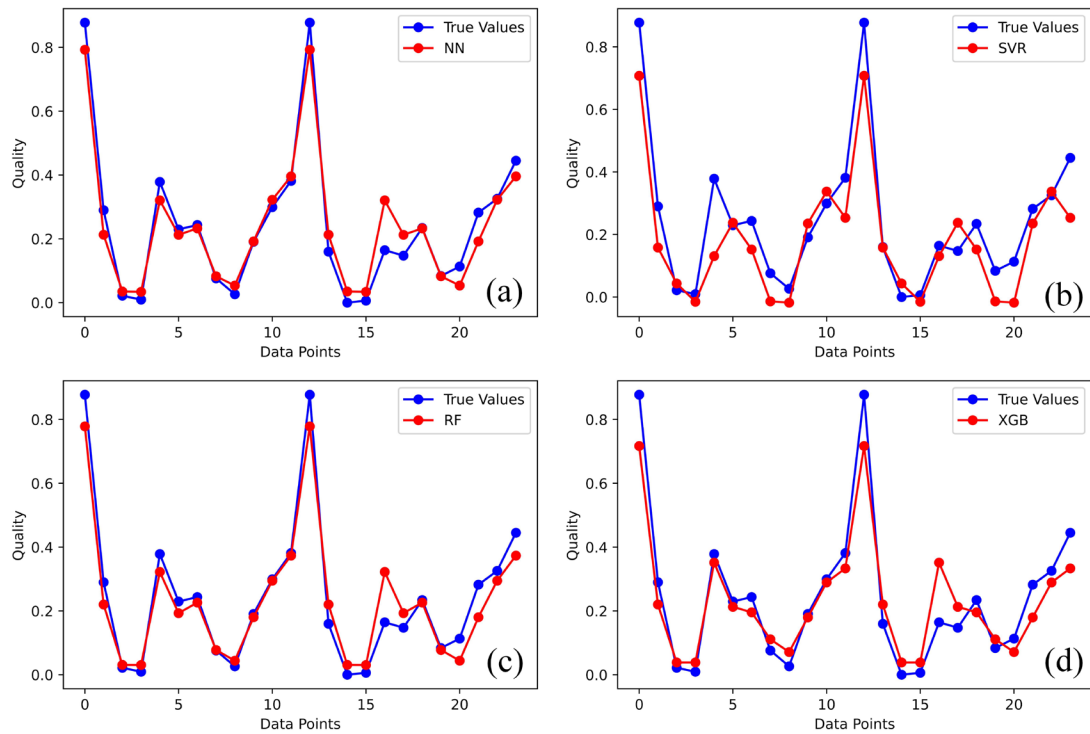
Table 5 shows 24 sample points from the test set (90 samples) used in this study. Fig. 9 presents a comparison between the actual experimental values and the predicted values using different machine learning techniques for these 24 sample points. Fig. 10 displays the deviations between the actual experimental values and the predicted values for the 24 sample points, with a 10% error line marked.

Table 6 Experimental test dataset (24 in 90)

No.	Normalized value			Input parameters			Output parameters
	Laser power	Laser Speed	Spacing	Laser power(P) (W)	Laser Speed(V) (mm/s)	Spacing (S)(μm)	
1	0.25	0.125	0.5	8	3	50	0.878
2	0.5	0.125	0.5	12	3	50	0.290
3	0.75	0.125	0.5	16	3	50	0.022

4	1	0.125	0.5	20	3	50	0.009
5	0.25	0	0.5	8	2	50	0.378
6	0.25	0.25	0.5	8	4	50	0.229
7	0.25	0.75	0.5	8	8	50	0.243
8	0.25	1	0.5	8	10	50	0.076
9	0.25	0.5	0	8	6	30	0.026
10	0.25	0.5	0.25	8	6	40	0.191
11	0.25	0.5	0.75	8	6	60	0.299
12	0.25	0.5	1	8	6	70	0.381
13	0.25	0.125	0.5	8	3	50	0.870
14	0.5	0.125	0.5	12	3	50	0.160
15	0.75	0.125	0.5	16	3	50	0
16	1	0.125	0.5	20	3	50	0.006
17	0.25	0	0.5	8	2	50	0.164
18	0.25	0.25	0.5	8	4	50	0.147
19	0.25	0.75	0.5	8	8	50	0.234
20	0.25	1	0.5	8	10	50	0.084
21	0.25	0.5	0	8	6	30	0.113
22	0.25	0.5	0.25	8	6	40	0.282
23	0.25	0.5	0.75	8	6	60	0.326
24	0.25	0.5	1	8	6	70	0.445

1



2

3

Fig. 10 Results of ML models on test set: (a) NN; (b) SVR; (c) RF ; (d)XGBoost

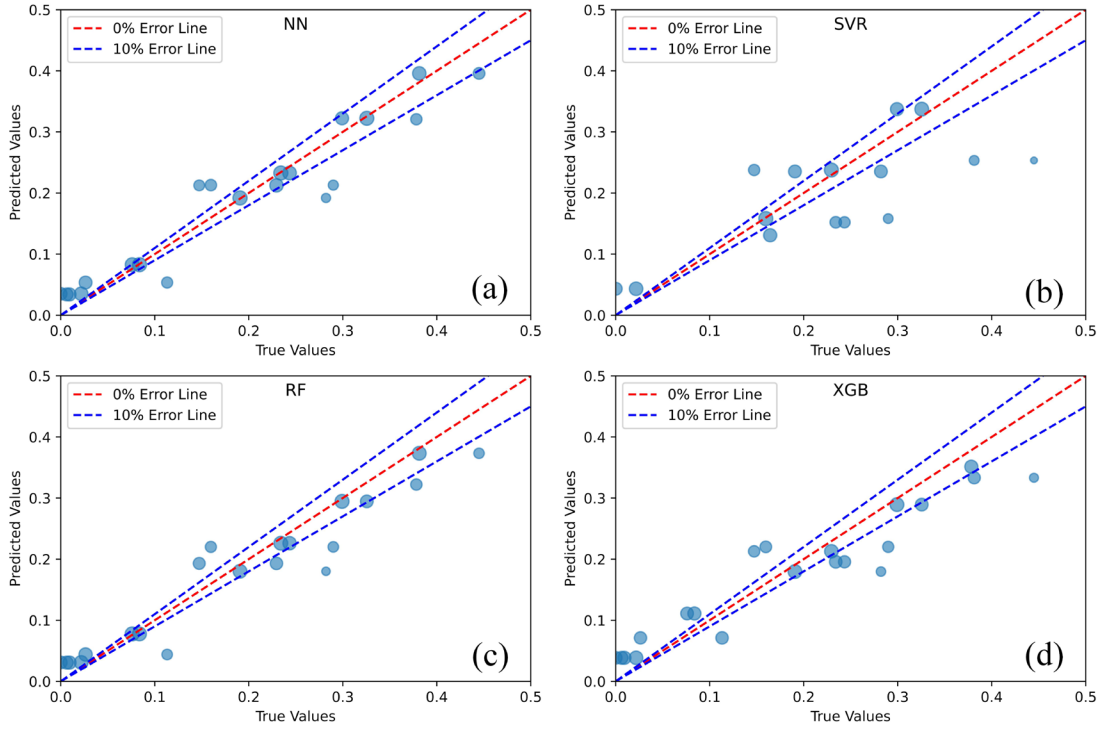


Fig. 11 Comparison between actual and predictions by ML models: (a) NN; (b) SVR; (c) RF ;
(d)XGBoost

Table 4, Fig. 9 and Fig. 10 shows that the network structure proposed in this work is effective for predicting the quality parameters of the small holes and has advantages compared to traditional machine learning models. However, an RMSE of 0.06-0.07 is acceptable for machining tasks because even with the same processing parameters, there will still be certain fluctuations results due to various factors, such as material properties, machine precision, environmental conditions, etc. In contrast, when a neural network is presented with a fixed set of processing parameters, its predictions are consistent and deterministic. A typical example is sample point 5 and sample point 17 in Table 5, which have the same parameters but exhibit a significant difference in quality parameters. Therefore, the RMSE cannot be reduced further. The network structure can also be more complex without considering the cost, but the purpose of this paper is to demonstrate how to recognize better processing parameters by neural networks and show its relationship to physical models, so this work just built up a basic model.

The advantage of neural networks is that it can process data fast. Using a neural network to query from power, speed, and fill spacing to quality parameters only takes 0.37 ms (CPU: AMD Ryzen 7 5800X, GPU: NVIDIA GeForce RTX 4090). To intuitively understand the knowledge learned by the neural network, this work chose 50 levels each for power, speed, and fill spacing. This formed $50 \times 50 \times 50 = 125000$ neural network prediction results, which took less than 1 minute. In fact, when the accuracy requirements are not very high, the selection of 50 levels of parameters is good enough in actual processing.

Parameter scanning range is: laser power 4–20 W, scanning speed 2–10 mm/s, fill spacing 30–70 μm . After generating 125,000 neural network prediction results, this work generated a heat cube where the three processing parameters are represented on the x, y, and z axes, and the quality parameters are represented by different color as the fourth axis. However, the drawback is that this visualization contains a large amount of information, making it difficult to analyze effectively.

To deal with this drawback, this work locked one processing parameter (generally locked in a typical value position, such as: fill spacing is 50 μm , the scanning speed is 6mm/s, and the laser power is 8 W). Then used the other two parameters as the x and y axes, and the machining quality parameters as the z-axis, and generated a three-dimensional heatmap, and at the -1 position of the z-axis, generated a contour map. This heatmap can display some of the knowledge learned by the neural network.

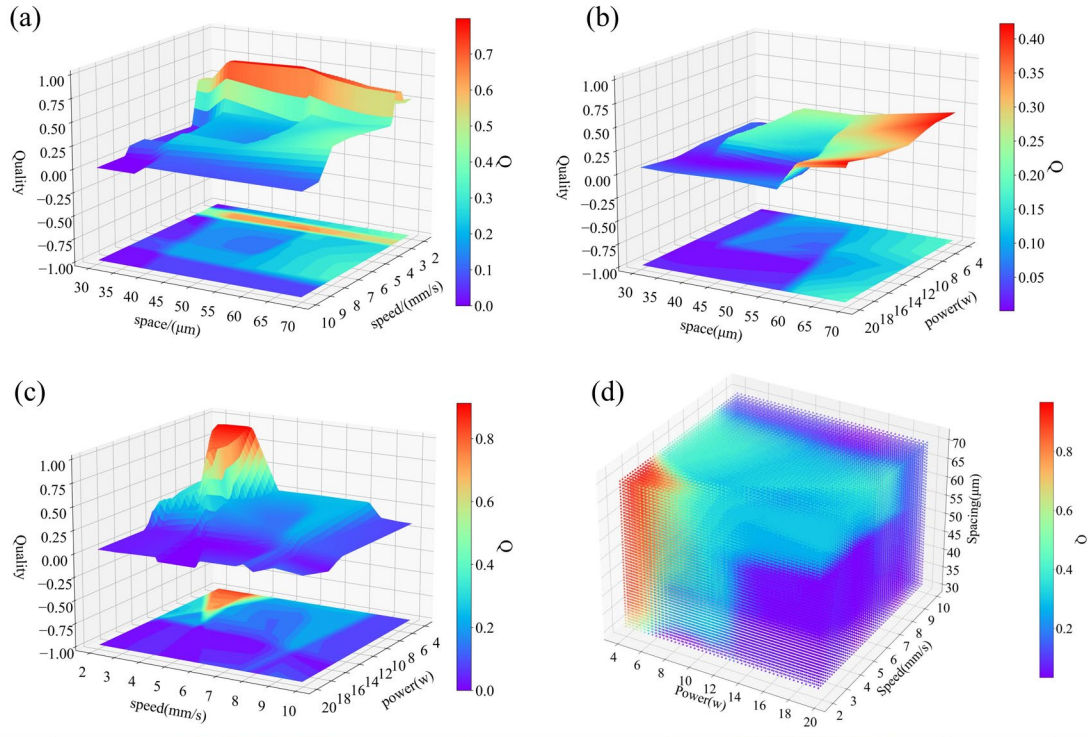


Fig. 12 Neural network based heat map and contour map

- (a) Effect of power and speed, (b) Effect of power and spacing, (c) Effect of speed and spacing,
- (d) Effect of power, speed and spacing.

The first heatmap is the effect of speed-spacing. In the low-velocity zone (2–4 mm/s) interval, the processing quality is poorer in all cases. As the fill spacing increases, more ring structures are generated, which aligns with expectation: the larger the laser fill spacing, the more surfaces are not irradiated. With increased speed, the processing quality parameters gradually improve in the high-speed region (4–10 mm/s). And the best processing quality is at small spacing (30–40 μm) & high-speed region (8–10 mm/s).

The second heatmap is about the power-spacing influence. Firstly, it shows that the processing situation is very good with high laser power (10–20W) and small spacing (30–55 μm) because it has strong energy to remove the material, and the small spacing ensures that the energy can irradiate the entire processing area. However, in the low-power laser (0–10W) part, the processing quality gradually deteriorates as the spacing increases and ring structures are produced. Only in the case of very small spacing (30–40 μm) can a better machining be achieved. This indicates that the machining spacing plays a dominant role in the machining quality, and this point can be validated in the subsequent physical simulations.

The third heat map shows the effect of power and speed on the processing quality. The processing quality is the worst when the pulse energy is low (0–10W) and the speed is about 3 mm/s. Keeping

the scanning speed constant and increasing laser power to 10–20 W can improve the processing quality –this indicates that in the high-power region (10–20 W), laser power plays a dominant role compared to scanning speed. The laser's ability to remove material increases when the power increases. However, when the pulse energy is low (0–10 W), as the processing speed increases, the processing quality gradually improves. This is a very interesting phenomenon because according to the physical model, increasing the scanning speed will lead to a shorter scanning time, leading to less heat flow and lower heat flux density, which usually results in poor processing quality. But this is exactly what makes neural networks interesting: they completely learn the parts of experimental data that do not match our cognition, which comes from real experimental results.

Another point is that this situation also exists in other laser processing research: the laser speed is not completely proportional to the processing depth, the material removal rate (MRR), or width during engraving (DeBastiani et al., 1990; Wei, 2022). The MRR shows a process of increasing and then decreasing with the laser scanning speed increasing, which is very similar to the rising process in experiment. For experiment, this situation may be due to the strong flushing effect of the water jet in the waterjet-guided laser: at low scanning speeds (2–3 mm/s), the water flow cannot timely carry away the particles and debris produced by the processed small holes, so the laser heat is absorbed by the impurities, resulting in inferior processing quality compared to the high-speed area (4–10 mm/s).

The significance of the heatmap is to understand the nonlinear contribution of the processing parameters to the quality parameters.

3.2 Optimization of processing parameters using neural networks

In order to select the appropriate processing parameters, it needs to determine the qualifying range of the quality parameters and then select them from the set of solutions calculated by the neural network.

Suppose the optimization parameters only have the quality parameter. To achieve better machining results (no ring and small wall taper), you only need to find the area where the quality parameter is as small as possible (<0.1), like the deepest blue/purple part in Fig. 11. Obviously, without consideration of the cost, choosing the maximum power, minimum spacing, and maximum speed can get the best quality.

In many processing tasks, such as drilling tasks, too much laser power may introduce a negative taper or bring material burn. So this work need to choose a metric to limit parameter selection and transform this current single-objective parameter optimization problem into a more complex multi-objective optimization problem. Consider two metrics: the quality parameter Q and the cost parameter C. The cost parameter C calculation function is:

$$f_{\text{cost}} = \frac{p_t}{p} \cdot \frac{v_t}{v} \cdot \frac{s_t}{s} \quad (11)$$

Where p_t , v_t , and s_t are typical filling spacing of 50 μm, scanning speed of 6 mm/s, and average power of 8 W. We are concerned with reaching the lowest quality parameter Q (<0.1) cost, with multiple sets of processing quality parameters, which is the conditional boundary. This multi-objective optimization problem with two objectives (the smallest quality parameter and the lowest processing cost) can be expressed as:

$$1 \quad \begin{cases} V - \min f(x) = [f_Q(p, v, s), f_{\text{cost}}(p, v, s)]^T \\ \text{s.t. } p \in [4, 20], v \in [2, 10], s \in [30, 70] \end{cases} \quad (12)$$

2 Where f_Q represents the quality parameter computed through the neural network. For multi-
 3 objective optimization problems (MOPs), the NSGA (Nondominated Sorting Genetic Algorithm)
 4 was proposed by Srinivas (Srinivas & Deb, 1994) to find the Pareto front solutions in high-
 5 dimensional spaces. It was further developed into the NSGA-II algorithm in 2002(Deb et al., 2002).
 6 Inspired by the natural process of biological evolution, evolutionary algorithms have shown
 7 advantages in solving complex optimization problems. In recent years, when addressing MOPs, the
 8 optimization algorithms must exhibit good convergence and consistency to accurately cover the
 9 Pareto front (Y. Wang et al., 2022; Zhou et al., 2023). In this part, this work chose a more intuitive
 10 way to create a new mixing parameter.

$$11 \quad K = C_{\text{cost}} \cdot \lambda + Q \cdot (1 - \lambda) \quad (13)$$

12 Where C_{cost} is the cost parameter, λ is the coefficient balancing the quality and cost parameters,
 13 and Q is the quality parameter. After determining the λ parameter, a new heat map can be generated
 14 based on K , and the new heat map can help us filter out better (both quality and cost) parameter
 15 choices. Firstly, take power, speed, and spacing as the x, y, and z axes. Then establish a cube using
 16 the f_Q , C_{cost} dataset, Q and K as its temperature parameters, as shown in Fig. 12 (d).

17 Many parameter combinations can achieve good processing quality in the model where only
 18 quality parameter Q is considered. However, in the model where Q and C are both considered, the
 19 number of parameter combinations that simultaneously balance quality and cost is limited. However,
 20 we can't see the parameter combinations inside the cube - they are still not intuitive enough. So, we
 21 lock one processing parameter to observe the parameter selection after introducing the cost
 22 parameter C_{cost} , as shown in Fig. 12 (a), (b), (c).

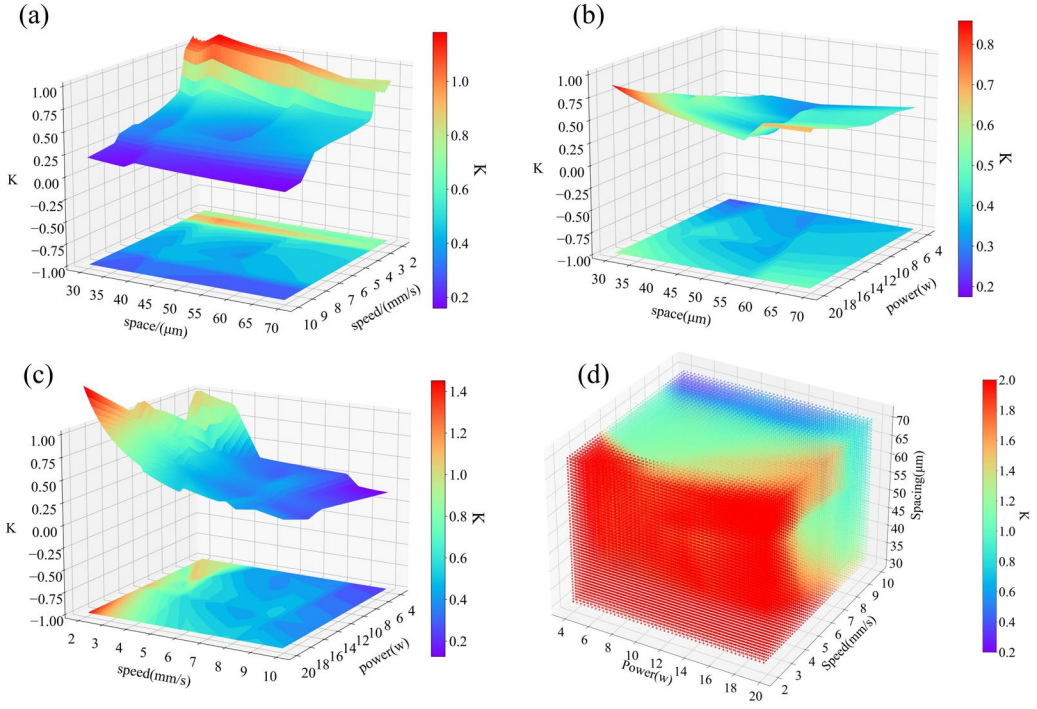


Fig. 13 (a)(b)(c) Heat map and contour map with mixing parameter K
 (d) heat cube with mixing parameter K

The darkest purple part indicates the better combination of parameters when considering the cost.
 Compared to Fig. 8, the choice of parameter combinations has been narrowed.

Here, we present the local optimal solutions obtained by using the GA algorithm while fixing one parameter (3 solutions) and one globally optimal solution (1 solution) without fixing any parameter in Table 7. Like Table 7, Table 5 shows the local optimal and global optimal solutions without considering the cost parameter. Table 6 shows the local worst and global worst solutions without considering the cost parameter. For those who want to produce high-quality holes, Table 5 can be referred to. If we need to create a hydrophobic structure in the shape of a circular mountain(Y. Zhang et al., 2022), Table 6 can be referred to.

Table 7 Optimal (best) parameters predicted by the neural network without cost

Prediction by NN	laser power(W)	Scanning Speed(mm/s)	Scanning Spacing(μm)	Machining quality
1	8.00	2.00	30.80	0.00
2	14.88	6.00	41.60	0.00
3	13.12	4.08	50.00	0.00
4	20.00	4.56	30.80	0.00

Table 8 Optimal (worst) parameters predicted by the neural network without cost

Prediction by NN	laser power(W)	Scanning Speed(mm/s)	Scanning Spacing(μm)	Machining quality
1	8.00	3.12	51.60	0.80
2	4.00	6.00	69.20	0.42

3	4.00	2.96	50.00	0.92
4	4.00	3.12	70.00	1.00

1 Table 9 Optimal (best) parameters predicted by the neural network with cost: $\lambda = 0.2$

Prediction by NN	laser power(W)	Scanning Speed(mm/s)	Scanning Spacing(μm)	K	Processing cost
1	8.00	9.92	69.60	0.16	0.43
2	4.00	6.00	33.20	0.16	0.75
3	4.00	9.92	50.00	0.12	0.30
4	4.00	9.84	38.80	0.08	0.39

2
3 It can be observed from Fig. 8(b) that among the processing parameter combinations with 6 mm/s
4 constant scanning speed, the one with a fill spacing of 70 μm , a scanning speed of 6 mm/s, and a
5 power of 4 W produces the worst quality. However, the processing quality improves as the power
6 increases and the fill spacing decreases. This trend will be verified in Section 3.3 using the physical
7 simulation model mentioned in Section 2.4
8

3.3 Validation using a physical simulation model

Purely relying on neural network parameters without the support of a physical model lacks convincing power. In this section, this work uses the physical simulation model established in section 2.4, which has power, scanning speed, and fill spacing as three input parameters. The software used is Comsol multiphysics, and the computing device (CPU: AMD Ryzen 7 5800X, 32GB memory).

The repetition frequency of the processing laser is 6 kHz with a pulse width of 240 ns. The simulation is a large deformation process in finite element simulation, which is difficult to loading and calculate heat source 6,000 times per second. Fortunately, the ring structure is formed near the processed surface, and the initial few pulses can form this structure. More pulses will expand the width and depth of the structure. Therefore, we can consider the situation that a small amount of pulse loading on the material surface and forms the structure.

Fig. 11 is a simulated image of waterjet-guided laser machining along a scanning line with a radius of 40 μm . It's the last scanning path when the power is 8 W, the spacing is 70 μm , and the speed is 6 mm/s. It shows the surface deformation after the first pulse of an 8 W laser, the cooling process between the first and second pulses, the surface after the second pulse, and the surface after the second pulse of a 16 W laser. Intense water cooling can quickly reduce the temperature of the machined surface before the arrival of the next pulse. Compared to the case of an 8 W laser, the annular groove produced by a 16 W laser is deeper, but the taper is smaller at the same depth.

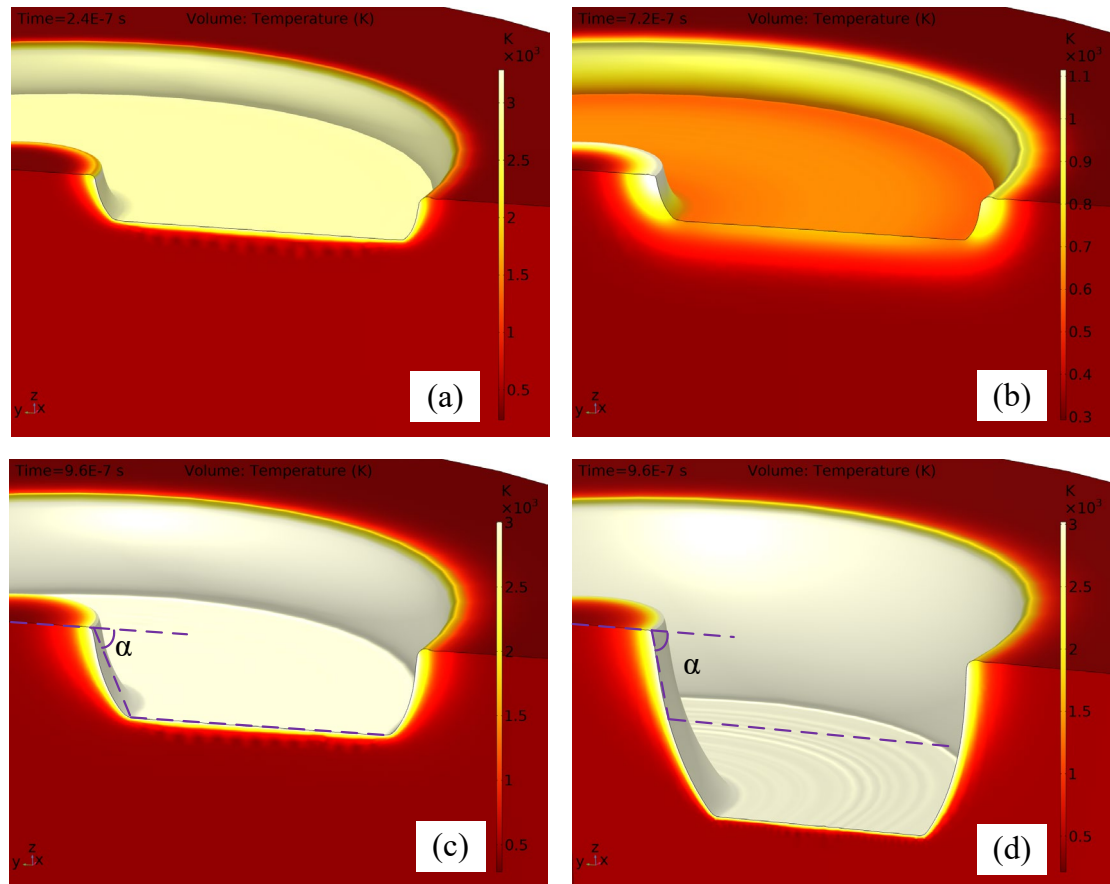


Fig. 14 The process of generating ring grooves

Let's first look at a parameter combination (filling spacing of 70 μm , scanning speed of 6mm/s, and power of 8 W) that can produce ring structures. Firstly, laser processing from the outside to the inside layer by layer, and the machining diameters are 500, 360, 220, and 80 μm . Because of the spacing (70 μm) is greater than the diameter of the waterjet-guided laser (50 μm). A part of the material (gray area)(see Fig. 13(a)) will not be scanned by the laser. The material will eventually produce a ring structure between the two scanning paths.

At the beginning of the laser action, the temperature of the first machining trajectory with a radius of r_1 rises sharply, forming a small rectangular groove. This is because the waterjet-guided laser in simulation is uniformly distributed (different from traditional Gaussian lasers). Then, the edge of the groove produces a positive taper due to heat conduction, like Fig. 12(a). As the initial taper of the groove exists, $\langle \vec{n}, \vec{e}_z \rangle$ in the heat source reduces the heat flux density on both sides of the groove.

After a long time of action, the rectangular groove gradually becomes like Fig. 12(b). It is worth noting that due to the extremely small time scale and the strong convective cooling effect of the waterjet-guided laser, the temperature of the material outside the machining area did not change significantly. After the machining is completed, the material is quickly cooled to room temperature. Fig. 12(b) and (c) show the machining process diagrams of the first and third channels and Fig. 12(d) shows the morphology after all the machining is completed and cooled.

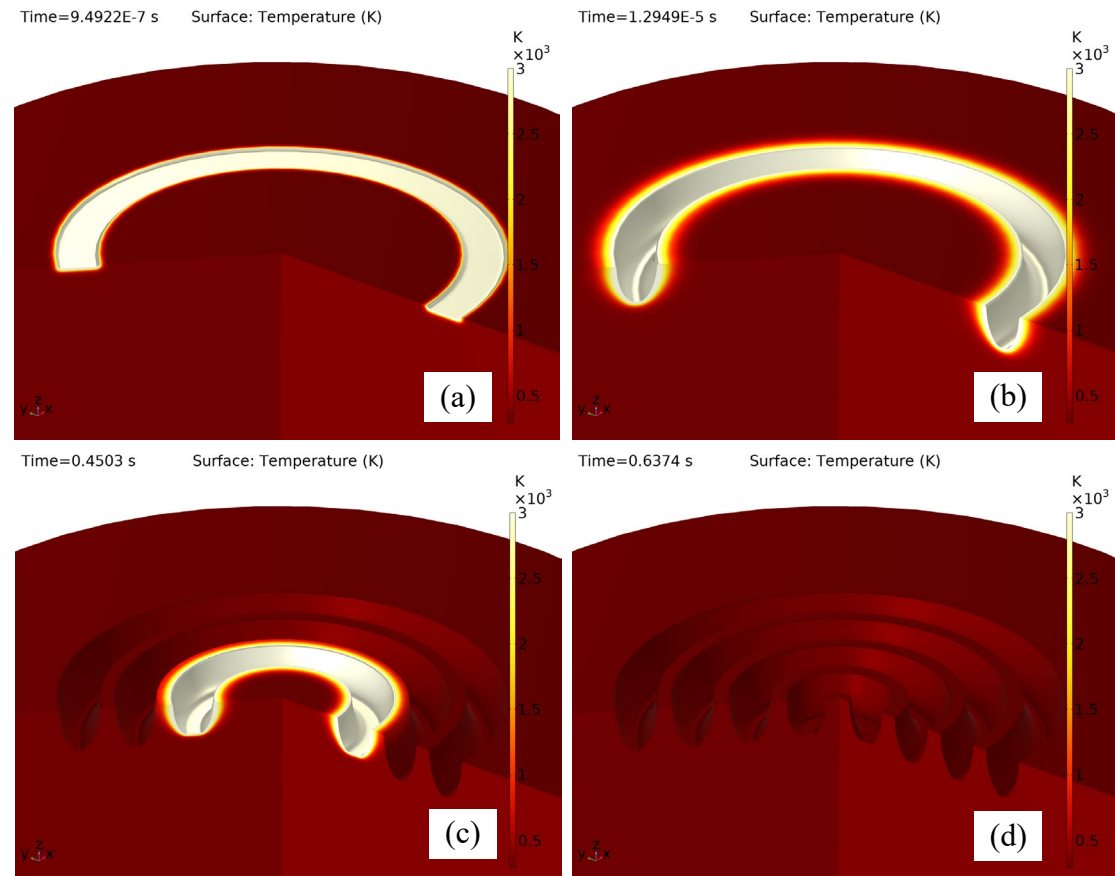


Fig. 15 Ring structure generation process

Fig. 13 (a), (b), (c), and (d)show the laser scanning path, optical microscope, and super-depth microscope images, and the comparison with simulation for a laser processing with a filling spacing

of 70 μm , a scanning speed of 6 mm/s, and an average power of 8 W. (8-6-70)

Comparing the processed images and simulation in Fig. 13(d) shows that the ring structure between the first and second processing lines disappeared. This may be because the waterjet-guided laser's high-pressure water jet (300 bar) violently washed away the outer structure. Similarly, the internal small cylindrical body also disappeared due to instability under the washing effect.

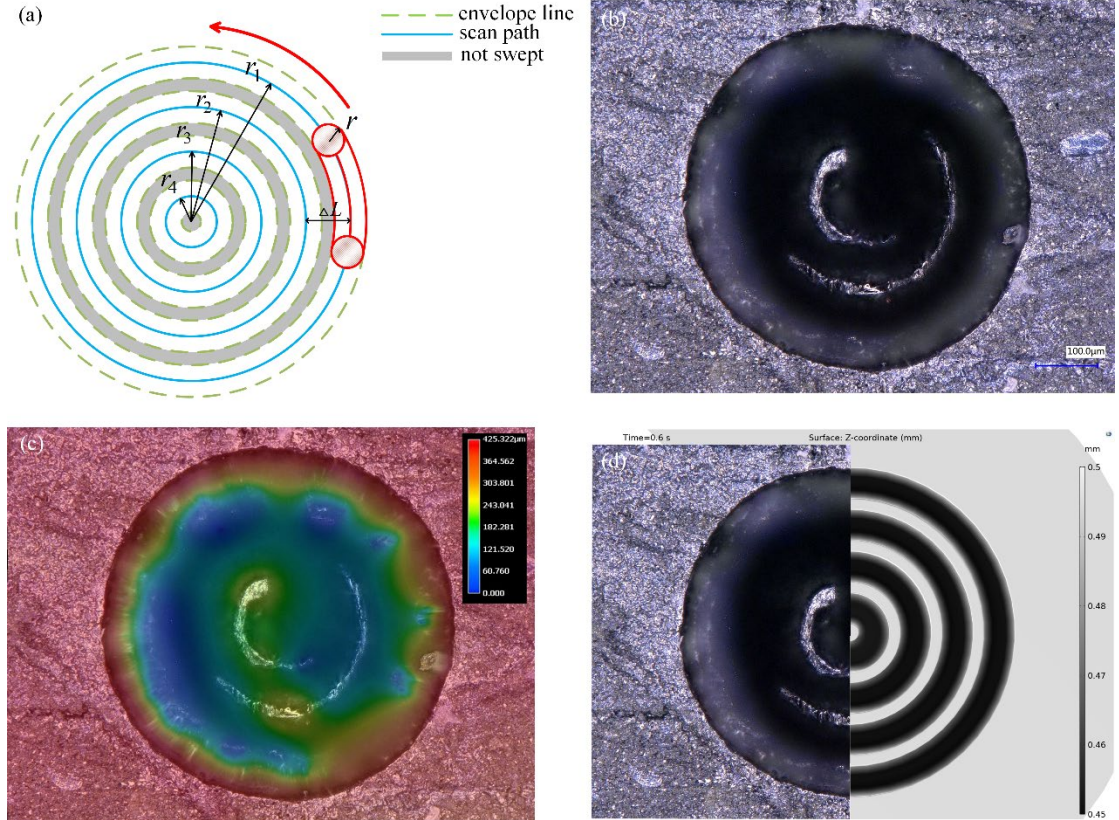


Fig. 16(a)scanning path, (b) optical microscope image, (c) super-depth microscope image, (d) comparison with ring structure simulation an optical microscope image.

One conclusion from Section 3.2 is that, with the power locked, poor machining results were obtained at scanning speeds between 3–3.5, while better machining results were obtained at higher scanning speeds. However, the simulation model established in this paper means that higher speeds result in shorter machining times, which leads to poor groove depth and ablation, contrary to the actual machining situation results. This may be because of the strong scouring and flow effects. Waterjet-guided lasers at high speeds can carry away debris. This nonlinear effect based on thermodynamics and deformation geometry is difficult to achieve with multiphysics fields that do not consider the molten silica flow(Y. Zhang et al., 2014) generated by the chemical reaction(J. Zhang et al., 2022). Therefore, this work locked the scanning speed at 6mm/s in the actual simulation and only discussed the influence of filling distance and power on the generation of ring structures. However, from another perspective, the neural network learned that finite element models could not simulate (counterintuitive) based on experimental results, which is important when facing more complex physical progress.

For the selected machining parameter combination in Section 3.2, this work chose a filling distance of 70 μm , a scanning speed of 6 mm/s, and a power of 5.6 W. Then change the filling distance (60 μm –50 μm –40 μm) and power (5.6 W, 8.8 W, 11 W) to observe the machining results.

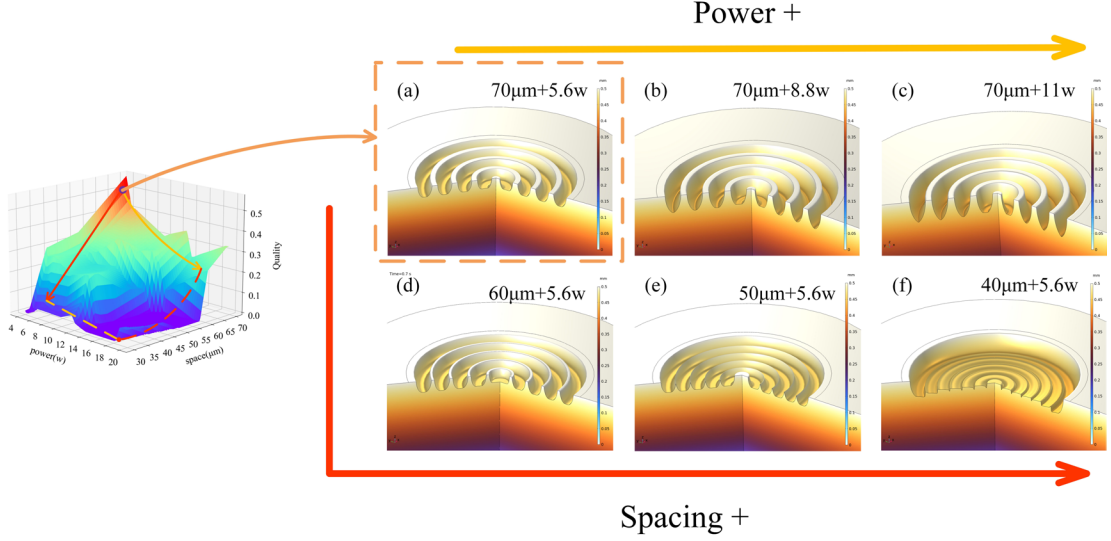


Fig. 17 Effect of different power and filling spacing on morphology

(a) 70 μm +5.6w (b) 70 μm +8.8w (c) 70 μm +11w (d) 60 μm +5.6w (e) 50 μm +5.6w (f) 40 μm +5.6w

In (a), (b), and (c) in Fig. 14, the depth of the small hole's burn increases, and the groove of the small hole becomes sharper as the laser power increases. The reason for the sharpness of the bottom groove of the small hole is due to the heat source term $\langle \vec{n}, \vec{e}_z \rangle$ in the heat source equation. Moreover, as the laser power increases, the taper of the small hole's wall gradually decreases at the same depth like Fig. 11(c) and(d), which can explain why the verticality of the hole wall is better at high laser powers.

In Fig. 14 (a), (d), (e), and (f), as the filling spacing decreases, the top of the ring structure gradually becomes thinner. Interestingly, if the filling distance is 50 μm , the entire machined surface should be uniformly irradiated by the flattened waterjet-guided laser, and intuitively, ring structures should not be produced. However, this very subtle ring structure is formed because the first scanning laser has already formed a rounded groove. And the second scanning laser scanning with the next round of laser will form these sharp annular mountains. These sharp annular mountains are lower than the annular mountains with a spacing parameter between 60–70 μm , and because they are very thin, most of them will be destroyed by the water flow. However, there are also a very small number of cases in dataset where annular mountain structures exist with a filling spacing of 50 μm .

When the spacing is 40 μm , a machining area has been irradiated twice, which has sunk in the simulation. However, there is no longer a ring structure and only a certain wall taper due to the low laser power.

Based on the phenomena and discussions in the physical simulation model, we have learned that the wall taper decreases for the same depth as laser power increases. As the filling spacing decreases, the formation of ring structures gradually disappears. However, even at a filling distance of 50 μm , some very thin circular structures still exist. Thus, this work have validated some of the knowledge learned by the neural network through the physical simulation model.

This work also has limitations: 1. This experiment only focused on the shallow surface structure; 2. Instead of using multiple individual quality features (e.g., taper, entrance/exit diameter, roughness,

1 etc.) for the quality features, a surface quality feature parameter incorporating ring structure and
2 hole wall taper was used as the parameter to be optimized. In the future, our work plan to further
3 address the above limitations. Once SiC/SiC composite materials and laser are standardized, a
4 relational database can be established for the quality parameters (depth, wall surface slope, entrance
5 and exit shape, surface roughness) and processing parameter combinations (energy, repetition
6 frequency, scanning speed, etc.). When selecting processing parameter combinations for different
7 quality requirements, the database can be referenced instead of extracting the relationship of the
8 result.

1 4. Conclusions

2 For SiCf/SiC composites, a waterjet-guided laser machining experiment was designed to
3 demonstrate the effects of laser power, scanning speed, and filling spacing on the quality parameter.
4 The machining results were digitized into quality parameters, and a neural network was established
5 to illustrate the relationship between machining parameters and machining quality parameters. A
6 simulation model was also established to explain some of the neural network's results. The overall
7 findings are as follows:

8 1. Even simple neural networks, with enough sample points (300), can achieve a relatively low
9 RMSE estimation (0.0668) and MAE estimation (0.0536) in mapping the relationship between
10 machining parameters and quality parameters. This is a significant advantage over some traditional
11 machine learning regression models (SVR, RF and XGBoost). Moreover, scanning the entire
12 parameter space can be completed in a short time, which is much faster than methods based on
13 physical models and parameter optimization methods.

14 2. Neural networks can learn some nonlinear data features that are difficult to represent in a
15 physical model, such as the influence of scanning speed on quality parameters in this experiment.
16 The coupling relationship between different machining and quality parameters can be explored
17 using appropriate data representation. In the experiment, to obtain good machining quality, it is
18 recommended to choose a smaller filling spacing (30–40 μm), larger power (14–20 W), and higher
19 speed (6–10 mm/s). If the task is to generate a special surface structure of a circular mountain, a
20 scanning speed of about 3 mm/s, smaller energy, and larger filling spacing (60–70 μm) could be
21 chosen. Introducing cost parameters in the optimization objective can consider both machining
22 quality parameters and costs.

23 3. Physical modeling simulation is essential, and when combined with neural networks, it can
24 help us deepen the understanding of the machining process. Some linear features and rules learned
25 by the neural network from the dataset can be validated in physical models, such as the impact of
26 laser power and filling spacing on structure generation, although some nonlinear features, such as
27 the influence of scanning speed on quality parameters, require more complex physical models (such
28 as physical simulation that considers material melt flow and water jet flow, water pressure, etc.) or
29 a deeper understanding of the laser machining process.

30 This study can serve as guidance for aerospace parts machining and provide an advanced
31 screening of process parameters when facing unknown new materials. It provides a shorter time for
32 selecting process parameters for the machining processes with specific analysis theory. It provides
33 a method of selecting process parameters based on processing results for the machining tasks, which
34 is difficult to explain and simulate by analysis theory, such as ultra-short pulse femtosecond laser
35 machining composite material.

1 **Author contributions**

2 **Mengxuan Gao:** Investigation, Methodology, Experimentation, Calculation, Writing - original
3 draft. **Songmei Yuan:** Supervision, Writing - review & editing, Funding acquisition. **Jiayong Wei:**
4 Investigation, Methodology, Experimentation. **Jin Niu:** Investigation, Methodology, Calculation.
5 **Zikang Zhang:** Investigation, Methodology. **Xiaoqi Li:** Physical simulation. **Jiaqi Zhang:**
6 Methodology. **Ning Zhou:** Methodology. **Mingrui Luo:** Methodology.

7 **Declaration of Competing Interest**

8 The authors declare that they have no known competing financial interests or personal relationships
9 that could have appeared to influence the work reported in this paper.

10 **Acknowledgements**

11 This work was supported by the Science Center for Gas Turbine Project (P2022-AB-IV-002-002).

12 **Data Availability Statement**

13 The data that support the findings of this study are available from the corresponding author upon
14 reasonable request.

15

16

1 References

- 2 An, Q., Chen, J., Ming, W., & Chen, M. (2021). Machining of SiC ceramic matrix composites: A
3 review. *Chinese Journal of Aeronautics*, 34(4), 540–567.
4 <https://doi.org/10.1016/j.cja.2020.08.001>
- 5 Bakhtiyari, A. N., Wang, Z., Wang, L., & Zheng, H. (2021). A review on applications of artificial
6 intelligence in modeling and optimization of laser beam machining. *Optics & Laser
7 Technology*, 135, 106721. <https://doi.org/10.1016/j.optlastec.2020.106721>
- 8 Bilal, A., Jahan, M., Talamona, D., & Perveen, A. (2018). Electro-Discharge Machining of Ceramics:
9 A Review. *Micromachines*, 10(1), 10. <https://doi.org/10.3390/mi10010010>
- 10 Casalino, G. (2018). [INVITED] Computational intelligence for smart laser materials processing.
11 *Optics & Laser Technology*, 100, 165–175. <https://doi.org/10.1016/j.optlastec.2017.10.011>
- 12 Casalino, G., Facchini, F., Mortello, M., & Mummolo, G. (2016). ANN modelling to optimize
13 manufacturing processes: The case of laser welding. *IFAC-PapersOnLine*, 49(12), 378–383.
14 <https://doi.org/10.1016/j.ifacol.2016.07.634>
- 15 Casalino, G., Losacco, A. M., Arnesano, A., Facchini, F., Pierangeli, M., & Bonserio, C. (2017).
16 Statistical Analysis and Modelling of an Yb: KGW Femtosecond Laser Micro-drilling
17 Process. *Procedia CIRP*, 62, 275–280. <https://doi.org/10.1016/j.procir.2016.06.111>
- 18 Chaki, S., Bose, D., & Bathe, R. N. (2020). Multi-Objective Optimization of Pulsed Nd: YAG Laser
19 Cutting Process Using Entropy-Based ANN-PSO Model. *Lasers in Manufacturing and
20 Materials Processing*, 7(1), 88–110. <https://doi.org/10.1007/s40516-019-00109-8>
- 21 Chen, J., An, Q., Ming, W., & Chen, M. (2021). Investigations on continuous-wave laser and pulsed

- laser induced controllable ablation of SiCf/SiC composites. *Journal of the European Ceramic Society*, 41(12), 5835–5849. <https://doi.org/10.1016/j.jeurceramsoc.2021.04.061>

Chen, L., Li, Y., Chen, G., Liu, X., & Liu, C. (2023). Physics-guided high-value data sampling method for predicting milling stability with limited experimental data. *Journal of Intelligent Manufacturing*. <https://doi.org/10.1007/s10845-023-02190-5>

Ciurana, J., Arias, G., & Ozel, T. (2009). Neural Network Modeling and Particle Swarm Optimization (PSO) of Process Parameters in Pulsed Laser Micromachining of Hardened AISI H13 Steel. *Materials and Manufacturing Processes*, 24(3), 358–368. <https://doi.org/10.1080/10426910802679568>

Deb, K., Pratap, A., Agarwal, S., & Meyarivan, T. (2002). A fast and elitist multiobjective genetic algorithm: NSGA-II. *IEEE Transactions on Evolutionary Computation*, 6(2), 182–197. <https://doi.org/10.1109/4235.996017>

DeBastiani, D. L., Modest, M. F., & Stubican, V. S. (1990). Mechanism of Material Removal from Silicon Carbide by Carbon Dioxide Laser Heating. *Journal of the American Ceramic Society*, 73(7), 1947–1952. <https://doi.org/10.1111/j.1151-2916.1990.tb05250.x>

Feng, S., Zhou, H., & Dong, H. (2019). Using deep neural network with small dataset to predict material defects. *Materials & Design*, 162, 300–310. <https://doi.org/10.1016/j.matdes.2018.11.060>

Gavalda Diaz, O., Garcia Luna, G., Liao, Z., & Axinte, D. (2019). The new challenges of machining Ceramic Matrix Composites (CMCs): Review of surface integrity. *International Journal of Machine Tools and Manufacture*, 139, 24–36. <https://doi.org/10.1016/j.ijmachtools.2019.01.003>

- 1 Goeke, A., & Emmelmann, C. (2010). Influence of laser cutting parameters on CFRP part quality.
- 2 *Physics Procedia*, 5, 253–258. <https://doi.org/10.1016/j.phpro.2010.08.051>
- 3 Goodfellow I, Bengio Y, & Courville A. (2016). *Deep learning*. Cambridge: MIT Press.
- 4 Hamrani, A., Agarwal, A., Allouhi, A., & McDaniel, D. (2023). Applying machine learning to wire
- 5 arc additive manufacturing: A systematic data-driven literature review. *Journal of*
- 6 *Intelligent Manufacturing*. <https://doi.org/10.1007/s10845-023-02171-8>
- 7 Heath, D. J., Grant-Jacob, J. A., Eason, R. W., & Mills, B. (2018). Single-pulse ablation of multi-
- 8 depth structures via spatially filtered binary intensity masks. *Applied Optics*, 57(8), 1904.
- 9 <https://doi.org/10.1364/AO.57.001904>
- 10 Heath, D. J., Grant-Jacob, J. A., Xie, Y., Mackay, B. S., Baker, J. A. G., Eason, R. W., & Mills, B.
- 11 (2018). Machine learning for 3D simulated visualization of laser machining. *Optics Express*,
- 12 26(17), 21574. <https://doi.org/10.1364/OE.26.021574>
- 13 Huang, X., Ng, W. L., & Yeong, W. Y. (2023). Predicting the number of printed cells during inkjet-
- 14 based bioprinting process based on droplet velocity profile using machine learning
- 15 approaches. *Journal of Intelligent Manufacturing*. <https://doi.org/10.1007/s10845-023-02167-4>
- 16 Jiang, P., Wang, C., Zhou, Q., Shao, X., Shu, L., & Li, X. (2016). Optimization of laser welding
- 17 process parameters of stainless steel 316L using FEM, Kriging and NSGA-II. *Advances in*
- 18 *Engineering Software*, 99, 147–160. <https://doi.org/10.1016/j.advengsoft.2016.06.006>
- 19 Kashinath, K., Mustafa, M., Albert, A., Wu, J.-L., Jiang, C., Esmaeilzadeh, S., Azizzadenesheli, K.,
- 20 Wang, R., Chattopadhyay, A., Singh, A., Manepalli, A., Chirila, D., Yu, R., Walters, R.,
- 21 White, B., Xiao, H., Tchelepi, H. A., Marcus, P., Anandkumar, A., ... Prabhat. (2021).

- 1 Physics-informed machine learning: Case studies for weather and climate modelling.
- 2 *Philosophical Transactions of the Royal Society A: Mathematical, Physical and*
- 3 *Engineering Sciences*, 379(2194), 20200093. <https://doi.org/10.1098/rsta.2020.0093>
- 4 Li, C.-F., Johnson, D. B., & Kovacevic, R. (2003). Modeling of waterjet guided laser grooving of
- 5 silicon. *International Journal of Machine Tools and Manufacture*, 43(9), 925–936.
- 6 [https://doi.org/10.1016/S0890-6955\(03\)00063-4](https://doi.org/10.1016/S0890-6955(03)00063-4)
- 7 Li, M., Zhang, J., Song, J., Li, Z., & Lu, S. (2023). A Clinical-Oriented Non-Severe Depression
- 8 Diagnosis Method Based on Cognitive Behavior of Emotional Conflict. *IEEE Transactions*
- 9 *on Computational Social Systems*, 10(1), 131–141.
- 10 <https://doi.org/10.1109/TCSS.2022.3152091>
- 11 Li, Z., Li, X., Zhang, B., Zhou, X., Liu, C., Jiang, Y., Zhen, C., Zheng, C., Zhang, L., & Cheng, L.
- 12 (2020). Enhanced thermal and mechanical properties of optimized SiCf/SiC composites
- 13 with in-situ CNTs on PyC interface. *Ceramics International*, 46(11), 18071–18078.
- 14 <https://doi.org/10.1016/j.ceramint.2020.04.126>
- 15 Liao, K., Wang, W., Mei, X., Tian, W., Yuan, H., Wang, M., & Wang, B. (2023). Shape regulation
- 16 of tapered microchannels in silica glass ablated by femtosecond laser with theoretical
- 17 modeling and machine learning. *Journal of Intelligent Manufacturing*, 34(7), 2907–2924.
- 18 <https://doi.org/10.1007/s10845-022-01950-z>
- 19 Loshchilov, I., & Hutter, F. (2019). *Decoupled Weight Decay Regularization* (arXiv:1711.05101).
- 20 arXiv. <http://arxiv.org/abs/1711.05101>
- 21 Manohar, B., & Das, R. (2022). Artificial Neural Networks for the Prediction of Monkeypox
- 22 Outbreak. *Tropical Medicine and Infectious Disease*, 7(12), 424.

- 1 https://doi.org/10.3390/tropicalmed7120424
- 2 Manohar, B., & Das, R. (2023). Artificial neural networks for prediction of COVID -19 in India by
- 3 using backpropagation. *Expert Systems*, 40(5), e13105. https://doi.org/10.1111/exsy.13105
- 4 McDonnell, M. D. T., Arnaldo, D., Pelletier, E., Grant-Jacob, J. A., Praeger, M., Karnakis, D., Eason,
- 5 R. W., & Mills, B. (2021). Machine learning for multi-dimensional optimisation and
- 6 predictive visualisation of laser machining. *Journal of Intelligent Manufacturing*, 32(5),
- 7 1471–1483. https://doi.org/10.1007/s10845-020-01717-4
- 8 Mills, B., Heath, D. J., Grant-Jacob, J. A., & Eason, R. W. (2018). Predictive capabilities for laser
- 9 machining via a neural network. *Optics Express*, 26(13), 17245.
- 10 https://doi.org/10.1364/OE.26.017245
- 11 Porter, J. A., Louhisalmi, Y. A., Karjalainen, J. A., & Füger, S. (2007). Cutting thin sheet metal with
- 12 a water jet guided laser using various cutting distances, feed speeds and angles of incidence.
- 13 *The International Journal of Advanced Manufacturing Technology*, 33(9–10), 961–967.
- 14 https://doi.org/10.1007/s00170-006-0521-7
- 15 Ren, Z., Zhen, X., Jiang, Z., Gao, Z., Li, Y., & Shi, W. (2023). Underactuated control and analysis
- 16 of single blade installation using a jackup installation vessel and active tugger line force
- 17 control. *Marine Structures*, 88, 103338. https://doi.org/10.1016/j.marstruc.2022.103338
- 18 Rong, Y., Zhou, Q., Huang, Y., Chang, Y., Zhang, G., & Shao, X. (2016). Multi-objective
- 19 optimization of laser brazing with the crimping joint using ANN and NSGA-II. *The*
- 20 *International Journal of Advanced Manufacturing Technology*, 85(5–8), 1239–1247.
- 21 https://doi.org/10.1007/s00170-015-8028-8
- 22 Samant, A. N., & Dahotre, N. B. (2009). Laser machining of structural ceramics—A review. *Journal*

- 1 of the European Ceramic Society, 29(6), 969–993.
- 2 <https://doi.org/10.1016/j.jeurceramsoc.2008.11.010>
- 3 Shen, Z. H., Zhang, S. Y., Lu, J., & Ni, X. W. (2001). Mathematical modeling of laser induced
4 heating and melting in solids. *Optics & Laser Technology*, 33(8), 533–537.
- 5 [https://doi.org/10.1016/S0030-3992\(01\)00005-6](https://doi.org/10.1016/S0030-3992(01)00005-6)
- 6 Srinivas, N., & Deb, K. (1994). Multiobjective Optimization Using Nondominated Sorting in
7 Genetic Algorithms. *Evolutionary Computation*, 2(3), 221–248.
- 8 <https://doi.org/10.1162/evco.1994.2.3.221>
- 9 Sun, D., Han, F., & Ying, W. (2019). The experimental investigation of water jet-guided laser cutting
10 of CFRP. *The International Journal of Advanced Manufacturing Technology*, 102(1–4),
11 719–729. <https://doi.org/10.1007/s00170-018-03218-4>
- 12 Wang, F., Bian, Y., Wang, H., Lyu, M., Pedrini, G., Osten, W., Barbastathis, G., & Situ, G. (2020).
13 Phase imaging with an untrained neural network. *Light: Science & Applications*, 9(1), 77.
- 14 <https://doi.org/10.1038/s41377-020-0302-3>
- 15 Wang, H., Zhou, X., Yu, J., Cao, Y., & Liu, R. (2010). Fabrication of SiCf/SiC composites by
16 chemical vapor infiltration and vapor silicon infiltration. *Materials Letters*, 64(15), 1691–
17 1693. <https://doi.org/10.1016/j.matlet.2010.05.013>
- 18 Wang, Y., Gao, W., Gong, M., Li, H., & Xie, J. (2022). A new two-stage based evolutionary
19 algorithm for solving multi-objective optimization problems. *Information Sciences*, 611,
20 649–659. <https://doi.org/10.1016/j.ins.2022.07.180>
- 21 Wei, J. (2022). Removal mechanism of SiC/SiC composites by underwater femtosecond laser
22 ablation. *Journal of the European Ceramic Society*, 11.

- 1 Wei, J., Yuan, S., Zhang, J., Zhou, N., Zhang, W., Li, J., An, W., Gao, M., & Fu, Y. (2022).
- 2 Femtosecond laser ablation behavior of SiC/SiC composites in air and water environment.
- 3 *Corrosion Science*, 9.
- 4 Xie, S., He, Z., Loh, Y. M., Yang, Y., Liu, K., Liu, C., Cheung, C. F., Yu, N., & Wang, C. (2023). A
- 5 novel interpretable predictive model based on ensemble learning and differential evolution
- 6 algorithm for surface roughness prediction in abrasive water jet polishing. *Journal of*
- 7 *Intelligent Manufacturing*. <https://doi.org/10.1007/s10845-023-02175-4>
- 8 Xie, Z., Chen, F., Wang, L., Ge, W., & Yan, W. (2023). Data-driven prediction of keyhole features
- 9 in metal additive manufacturing based on physics-based simulation. *Journal of Intelligent*
- 10 *Manufacturing*. <https://doi.org/10.1007/s10845-023-02157-6>
- 11 Yang, J., Zeng, B., Ni, Z., Fan, Y., Hang, Z., Wang, Y., Feng, C., & Yang, J. (2023). Comparison of
- 12 traditional and automated machine learning approaches in predicting the compressive
- 13 strength of graphene oxide/cement composites. *Construction and Building Materials*, 394,
- 14 132179. <https://doi.org/10.1016/j.conbuildmat.2023.132179>
- 15 Yang, L., & Shami, A. (2020). On hyperparameter optimization of machine learning algorithms:
- 16 Theory and practice. *Neurocomputing*, 415, 295–316.
- 17 <https://doi.org/10.1016/j.neucom.2020.07.061>
- 18 Yousef, B. F., Knopf, G. K., Bordatchev, E. V., & Nikumb, S. K. (2003). Neural network modeling
- 19 and analysis of the material removal process during laser machining. *The International*
- 20 *Journal of Advanced Manufacturing Technology*, 22(1–2), 41–53.
- 21 <https://doi.org/10.1007/s00170-002-1441-9>
- 22 Zhang, J., Yuan, S., Wei, J., Li, J., Zhang, Z., Zhang, W., & Zhou, N. (2022). Spatio-temporal multi-

- 1 scale observation of the evolution mechanism during millisecond laser ablation of SiCf/SiC.
- 2 *Ceramics International*, 48(16), 23885–23896.
- 3 <https://doi.org/10.1016/j.ceramint.2022.05.057>
- 4 Zhang, Y. (2023). Applications of machine learning in metal powder-bed fusion in-process
- 5 monitoring and control: Status and challenges. *Journal of Intelligent Manufacturing*.
- 6 Zhang, Y., & Ling, C. (2018). A strategy to apply machine learning to small datasets in materials
- 7 science. *Npj Computational Materials*, 4(1), 25. <https://doi.org/10.1038/s41524-018-0081-z>
- 9 Zhang, Y., Qiao, H., Zhao, J., & Cao, Z. (2022). Surface topography by water jet-guided laser
- 10 texturing on wettability of monocrystalline silicon. *The International Journal of Advanced*
- 11 *Manufacturing Technology*, 120(3–4), 2747–2761. <https://doi.org/10.1007/s00170-022-08712-4>
- 13 Zhang, Y., Shen, Z., & Ni, X. (2013). *Numerical simulation of melt ejection during the laser drilling*
- 14 *process on metal by millisecond pulsed laser* (S. Kaierle, J. Liu, & J. Cao, Eds.; p. 87962I).
- 15 <https://doi.org/10.1111/12.2009965>
- 16 Zhang, Y., Shen, Z., & Ni, X. (2014). Modeling and simulation on long pulse laser drilling
- 17 processing. *International Journal of Heat and Mass Transfer*, 73, 429–437.
- 18 <https://doi.org/10.1016/j.ijheatmasstransfer.2014.02.037>
- 19 Zhou, X., Cai, X., Zhang, H., Zhang, Z., Jin, T., Chen, H., & Deng, W. (2023). Multi-strategy
- 20 competitive-cooperative co-evolutionary algorithm and its application. *Information*
- 21 *Sciences*, 635, 328–344. <https://doi.org/10.1016/j.ins.2023.03.142>
- 22